Overcoming volumetric locking in material point methods

William M. Coombs*, Tim J. Charlton, Michael Cortis, Charles E. Augarde

Department of Engineering, Durham University, Science Site, South Road, Durham, DH1 3LE, UK

Highlights

- The proposed formulation overcomes finite deformation volumetric locking for near-incompressible non-linear solid mechanics.
- The method is applicable to all existing material point methods.
- No restriction is placed on the constitutive model.
- Quasi-static implicit implementation ensures asymptotic quadratic convergence.
- The formulation reduces spurious stress oscillations.

Abstract

Material point methods suffer from volumetric locking when modelling near incompressible materials due to the combination of a low-order computational mesh and large numbers of material points per element. However, large numbers of material points per element are required to reduce integration errors due to non-optimum placement of integration points. This restricts the ability of current material point methods in modelling realistic material behaviour.

This paper presents for the first time a method to overcome finite deformation volumetric locking in standard and generalised interpolation material point methods for near-incompressible non-linear solid mechanics. The method does not place any restriction on the form of constitutive model used and is straightforward to implement into existing implicit material point method codes. The performance of the method is demonstrated on a number of two and three-dimensional examples and its correct implementation confirmed through convergence studies towards analytical solutions and by obtaining the correct order of convergence within the global Newton–Raphson equilibrium iterations. In particular, the proposed formulation has been shown to remove the over-stiff volumetric behaviour of conventional material point methods and reduce stress oscillations. It is straightforward to extend this approach to other material point methods and the presented formulation can be incorporated into all existing material point methods available in the literature.

---

* Corresponding author.
E-mail address: w.m.coombs@durham.ac.uk (W.M. Coombs).

1. Introduction

Lagrangian mesh-based methods dominate engineering numerical computations in solid mechanics. However, for problems involving large deformations there are issues with pure Lagrangian formulations related to mesh distortion which impact on the accuracy and stability of the methods. With these methods it is therefore necessary to re-mesh and map state variables between the discretisations. One alternative numerical technique that has been demonstrated to be applicable to problems involving very large deformations is the material point method. The material point method was developed by Sulsky et al. [1] as a solid mechanics extension to the fluid implicit particle method [2] which itself was developed from the particle-in-cell method [3]. In the material point method, computations take place on a background grid but the calculations are based on information (stress, state variables, etc.) held at material points that are convected through the background grid as the material deforms. This allows computations to take place on an undistorted background mesh whilst modelling problems involving very large deformations. The simplest way to summarise the material point method is: a finite element method where the integration points (material points) are allowed to move independently from the mesh.

Allowing the material points to move through the background grid reduces the accuracy of the integration required to map information between the material points and the background grid [4]. Therefore, material point methods typically use more material points per element than would be adopted if the elements were integrated using Gauss–Legendre quadrature. Combining this with the fact that material point methods generally use a low order background grid (bi-linear quadrilaterals or tri-linear hexahedrals are a common choice) means that the method is susceptible to volumetric locking (resulting in over-stiff behaviour) when modelling near-incompressible materials. This volumetric locking is caused by excessive constraints placed on an element's deformation by the points used to integrate the stiffness of the element. That is, the constitutive model will require near-isochoric behaviour at the integration (or material) point's location within the element and each of these points places a constraint on the deformation of the element. At a specific number of points the element will lock, resulting in over-stiff behaviour, where the number of points to cause locking is linked to the basis of the element.

A common (and successful) technique to avoid volumetric locking in finite element methods is to use higher order elements with reduced Gaussian integration. However, this is not viable in the material point method, primarily due to the fact that at each step of a material point method analyses it is not known how many material points will be in any given element. In the context of finite deformation solid mechanics, a number of formulations have been proposed to overcome volumetric locking within finite elements, these include: mixed variational methods [5], mixed displacement-pressure formulations [6], geometrically non-linear $\bar{B}$ approaches [7], enhanced assumed strain elements [8–10], co-rotational approaches [11], $\bar{F}$ formulations [12,13] and finite deformation selective reduced integration methods [14], amongst others. See de Souza Neto et al. [15] or de Borst et al. [16] for more detailed reviews of the available methods.

To date the issue of volumetric locking in material point methods has mainly been focused on the analysis of fluid mechanics problems (see for example Zhang et al. [17] and the references contained within), with the notable exception of Mast et al. [18]. Mast et al. [18] investigated the issue of kinematic (volumetric and shear) locking in the material point method and developed a Hu–Washizu multi-field variational principle based approach which introduces independent approximations for the volumetric and the deviatoric components of the strain and stress fields. Although the approach has been shown to overcome volumetric locking in dynamic fluid and solid mechanics problems, it significantly increases the size of the linear system, introduces additional non-physical variables and was only demonstrated for linear material behaviour.

This paper presents for the first time a method to overcome finite deformation volumetric locking in standard and generalised interpolation material point methods for near-incompressible non-linear solid mechanics. In the standard material point method the material points act as discrete lumped masses and only interact with the element that they are located within whereas in the generalised interpolation method each material point has an associated domain which interacts with any elements that it overlaps. To overcome the issue of volumetric locking we adopt the $\bar{F}$ approach of de Souza Neto et al. [12] for the following reasons: (i) unlike mixed approaches it does not introduce any additional unknowns into the linear system, (ii) it is simple to implement within existing finite element codes (and therefore material point codes), (iii) the approach can be used with any constitutive model, (iv) it does not introduce any additional *tuning* parameters into the code and (v) it does not introduce any additional material points to track the volumetric behaviour.

The layout of the paper is as follows, Section 2 details the adopted material point formulation including both the standard and generalised interpolation material point methods. Section 3 details the modifications required to overcome volumetric locking, including details on the numerical implementation. Numerical examples are presented in Section 4 and, finally, conclusions are drawn in Section 5.

The majority of the mathematical development in the paper is presented in tensor form using index notation, the notable exception is the numerics that are presented in matrix–vector form for ease of implementation.

2. Material point formulation

This section details the quasi-static implicit finite deformation elasto-plastic material point method formulation adopted in this paper. The formulation is largely based on Charlton et al. [19] but with the resulting discrete equations formulated point-wise rather than element-wise. The section starts with the continuum problem statement before detailing the discrete material point formulation, boundary conditions, basis functions and domain updating. Finally the computational procedure is outlined.

2.1. Continuum problem statement

In this paper we restrict the problem to that of isotropic finite deformation elasto-plasticity defined by the following updated Lagrangian weak statement of equilibrium

$$\int_{\varphi_t(\Omega)} \Big(\sigma_{ij}(\nabla \eta)_{ij} - b_i \eta_i \Big) \mathrm{d}v - \int_{\varphi_t(\partial \Omega)} \Big(t_i \eta_i \Big) \mathrm{d}s = 0. \tag{1}$$

φ_t is the motion of the material body with domain, Ω, which is subjected to tractions, t_i, on the boundary of the domain (with surface, s), $\partial \Omega$, and body forces, b_i, acting over the volume, v of the domain, which lead to a Cauchy stress field, σ_{ij}, through the body. The weak form is derived in the current frame assuming a field of admissible virtual displacements, η_i. Within this updated Lagrangian formulation we adopt a multiplicative decomposition of the deformation gradient into elastic and plastic components combined with a linear relationship between elastic logarithmic strains and Kirchhoff stresses. This formulation is one of the most straightforward ways of implementing large strain elasto-plasticity within a finite element framework as it allows conventional small-strain constitutive formulations to be used without modification [20,21]. The finite deformation framework adopted in this paper is based on the implementations given in Simo [20], de Souza Neto et al. [15], Coombs et al. [22], Coombs [23], Charlton et al. [19], amongst others. It is also possible to extend the formulation to allow for both elastic and plastic anisotropies [24] although here we restrict the material formulation to isotropic behaviour.

Within the context of finite deformation mechanics, the deformation gradient, F_{ij} provides the fundamental link between the original and deformed configurations

$$F_{ij} = \frac{\partial x_i}{\partial X_j}, \tag{2}$$

where X_i are the original (reference) coordinates and $x_i = \varphi(X_i, t)$ are the updated coordinates in the current (deformed) body. As stated previously, we assumed that the deformation gradient can be multiplicatively decomposed into elastic and plastic components [25,26]

$$F_{ij} = F^{\mathrm{e}}_{ik} F^{\mathrm{p}}_{kj}, \tag{3}$$

where the superscripts e and p denote the elastic and plastic components. In this paper we adopt logarithmic strains and Kirchhoff stresses and combine these measures with an exponential map of the plastic flow rule to allow the use of conventional small-strain stress integration algorithms with a finite deformation framework.[1] This is a powerful combination as it allows existing constitutive formulations to be used directly rather than reformulating them for the particular choice of stress and strain measures used in the large deformation mechanics.

The elastic logarithmic strain is defined as

$$\varepsilon^{\mathrm{e}}_{ij} = \frac{1}{2} \ln \big(b^{\mathrm{e}}_{ij} \big), \qquad \text{where} \qquad b^{\mathrm{e}}_{ij} = F^{\mathrm{e}}_{ik} F^{\mathrm{e}}_{jk} \tag{4}$$

---

[1] Details on the recovery of the small strain format of stress integration can be found in de Souza Neto et al. [15], Coombs [23], amongst others.

is the left elastic Cauchy–Green strain and the Kirchhoff stress, τ_{ij}, can be obtained using

$$\tau_{ij} = D^{\text{e}}_{ijkl}\varepsilon^{\text{e}}_{kl}, \tag{5}$$

where D^{e}_{ijkl} is the linear elastic stiffness matrix. The Cauchy stress can be obtained from the Kirchhoff stress through

$$\sigma_{ij} = \frac{1}{J}\tau_{ij}, \qquad \text{where} \qquad J = \det(F_{ij}) \tag{6}$$

is the volume ratio between the deformed and reference configurations.

In order to advance the non-linear solution, the finite deformation equations are discretised in pseudo-time by imposing the deformation over a number of load (or pseudo-time) steps. This allows the current deformation gradient to be defined using

$$F_{ij} = \Delta F_{ik}(F_n)_{kj}, \tag{7}$$

where ΔF_{ij} is the increment in the deformation gradient between the previously converged state, denoted using a subscript n, and the current state. In order to obtain the updated Kirchhoff stress state for the current deformation gradient, a constitutive model requires an initial estimate (or trial) of the elastic strain (or stress) state. In this approach the trial elastic Cauchy–Green strain tensor is given by

$$(b^{\text{e}}_t)_{ij} = \Delta F_{ik}(b^{\text{e}}_n)_{kl}\Delta F_{jl}, \tag{8}$$

where the subscript t denotes a quantity defined in the trial state. The previous elastic Cauchy–Green strain tensor, $(b^{\text{e}}_n)_{ij}$, can be obtained from the previous elastic strain state through

$$(b^{\text{e}}_n)_{ij} = \exp\Big(2(\varepsilon^{\text{e}}_n)_{ij}\Big) \tag{9}$$

and the trial elastic strain state follows as

$$(\varepsilon^{\text{e}}_t)_{ij} = \frac{1}{2}\ln\Big((b^{\text{e}}_t)_{ij}\Big). \tag{10}$$

The adopted constitutive algorithm can then be used to return the updated elastic strain, $\varepsilon^{\text{e}}_{ij}$, and Kirchhoff stress, τ_{ij}, states.

2.2. Discrete material point implementation

The displacements across the domain are discretised according to

$$\varphi_i = \sum_{v=1}^{n}(S_{vp})(d_i)_v \qquad \text{and} \qquad \eta_i = \sum_{v=1}^{n}(S_{vp})(d^{\eta}_i)_v, \tag{11}$$

where S_{vp} are the shape functions that link the element vertices, v, and the material points, p. d_i and d^{η}_i are the physical and virtual nodal displacements and n is the number of nodes that influence the point of interest.

The Galerkin form of the weak statement of equilibrium over each background grid element, E, can be obtained from (1) and (11) as

$$\{f^R\} = \int_{\varphi_t(E)}[G]^T\{\sigma\}\mathrm{d}v - \int_{\varphi_t(E)}[S_{vp}]^T\{b\}\mathrm{d}v - \int_{\varphi_t(\partial E)}[S_{vp}]^T\{t\}\mathrm{d}s = \{0\}, \tag{12}$$

where $[G]$ is the tensorial form of the strain–displacement matrix containing derivatives of the shape functions with respect to the updated coordinates (see Section 2.4). The first term in (12) is the internal force within an element and the combination of the second and third terms is the external force vector. Eq. (12) is non-linear in terms of the unknown nodal displacements and can be efficiently solved using the standard Newton–Raphson (N–R) procedure. The nodal displacements within a load step, $\{\Delta d\}$, can be obtained by iteratively updating the nodal displacements until (12) is satisfied within a given tolerance using

$$\{\delta d_k\} = [K]^{-1}\{f^R_{k-1}\}, \tag{13}$$

where k is the current iteration within the loadstep, $[K]$ is the global stiffness matrix and $\{\delta d_k\}$ is the iterative increment in the displacements from that iteration. $\{f^R_{k-1}\}$ is the residual out of balance force vector associated with the previous

displacement value; the difference between the internal forces due to the Cauchy stresses within the material and the applied boundary conditions. The current displacement in a loadstep can be obtained by summing the iterative increments within the loadstep, that is

$$\{\Delta d_k\} = \sum_{n=1}^{k} \{\delta d_n\},$$ (14)

where it is assumed that $\{\delta d_0\} = \{0\}$. The global stiffness matrix can be obtained by linearising the discrete statement of equilibrium with respect to the unknown nodal displacements to give

$$[k^E] = \int_{\varphi_t(E)} [G]^T [A][G] \mathrm{d}v.$$ (15)

In (15), $[A]$ is the spatial consistent tangent modulus for a point within the element

$$A_{ijkl} = \frac{1}{2J} D_{ijmn}^{\mathrm{alg}} L_{mnpq} B_{pqkl} - S_{ijkl},$$ (16)

where

$$L_{mnpq} = \frac{\partial \ln(b_{mn}^{\mathrm{e}})}{\partial b_{pq}^{\mathrm{e}}}, \qquad B_{pqkl} = \delta_{pk} b_{ql}^{\mathrm{e}} + \delta_{qk} b_{pl}^{\mathrm{e}}, \qquad S_{ijkl} = \sigma_{ij} \delta_{jk}$$ (17)

and D_{ijmn}^{alg} is the small-strain algorithmic tangent obtained from the constitutive model. This tangent is the linearisation of the stress integration algorithm and ensures that asymptotic quadratic convergence is obtained in the global N–R iterations [27]. The derivative of the logarithm of the elastic Cauchy–Green strain tensor with respect to its argument is a special case of the more general formulation given by Miehe [28]. Note that all of the components of A_{ijkl} should be evaluated in the spatial frame, i.e. the current deformed configuration.

In material point methods the physical domain is discretised by a number of material points. These points are used to numerically approximate the stiffness (15) of the elements in the background mesh, essentially replacing the conventional Gauss points (or other integration method). The key difference between material point and finite element methods is that these integration points move relative to the background mesh rather than being directly coupled to the positions of the background grid nodes. The stiffness contribution of a single material point to the background mesh is

$$[k_p] = [G]^T [A][G] V_p,$$ (18)

where V_p is the volume associated with the material point in the spatial (updated) frame

$$V_p = \det\left(\Delta F_{ij}\right) V_p^n = \det\left(F_{ij}\right) V_p^0,$$ (19)

where V_p^n and V_p^0 are the volume associated with the previously converged state and the initial configuration, respectively. The internal force contribution of a single material point to the background mesh is

$$\{f^p\} = [G]^T \{\sigma\} V_p.$$ (20)

Following the work of Charlton et al. [19], the increment in the deformation gradient is obtained from

$$\Delta F_{ij} = \delta_{ij} + \frac{\partial \Delta u_i}{\partial \tilde{X}_j} = \delta_{ij} + \sum_{v=1}^{n} (\Delta u_i)_v \frac{\partial (S_{vp})}{\partial \tilde{X}_j},$$ (21)

where Δu_i is the displacement increment within the current loadstep, $\tilde{X}_j$ are the coordinates at the start of the loadstep and n is the number of nodes that influence the material point. This allows the increment in the deformation gradient to be obtained from derivatives of the basis functions based on the coordinates of the nodes at the start of the loadstep. This is essential as in material point methods there is no concept of the current (deformed) nodal coordinates as information is lost between incremental steps. Also, the basis functions for material point methods are typically only defined on a regular background grid. The spatial derivatives of the basis functions can subsequently be calculated using the method proposed by Charlton et al. [19], that is

$$\frac{\partial (S_{vp})}{\partial x_j} = \frac{\partial (S_{vp})}{\partial \tilde{X}_i} \frac{\partial \tilde{X}_i}{\partial x_j} = \frac{\partial (S_{vp})}{\partial \tilde{X}_i} \left(\Delta F_{ij}\right)^{-1}.$$ (22)

It is essential that the spatial derivatives are used in strain–displacement matrix, $[G]$, to both ensure the correct order of convergence in the N–R process and convergence towards the correct solution based on the partial internal force contribution, (20).

2.3. External loads & boundary conditions

The body force in (12) is approximated by

$$\{f_b^p\} = [S_{vp}]^T\{b\}V_p,\tag{23}$$

where $\{b\}$ is the body force associated with the material point. In this paper we ignore the external tractions as their general implementation within material points has yet to be fully clarified due to the uncertain definition of the boundary of the physical domain.[2]

In this paper, Dirichlet boundary conditions are imposed directly on the background mesh in the same way as the standard finite element method. This places some restrictions on the form of the boundary conditions that can be applied to the material point method, which have been overcome by the recent work of Cortis et al. [29], however the focus of this paper is on volumetric locking rather than general boundary condition imposition.

2.4. Basis functions

We assume that the background finite element grid consists of regular two-dimensional bi-linear quadrilateral or three-dimensional tri-linear hexahedral elements with their edges aligned with the global Cartesian coordinates. In [19] an implicit formulation of the generalised interpolation material point method was presented where the basis functions were defined locally over each element. Here we follow a different approach and define the basis functions based on the global positions of the background grid nodes and the material points.

The basis functions for standard and generalised interpolation material point methods can be expressed as

$$S_{vp} = \frac{1}{V_p^n}\int_{\Omega_p}\chi_p N_v(\tilde{X}_p)dx,\tag{24}$$

where Ω_p is the influence domain associated with the material point, χ_p is the characteristic function associated with the material point, V_p^n is the volume associated with the material point at the start of the loadstep, N_v are the underlying shape functions of the finite element grid which are dependent on the position of the material point at the start of the loadstep, $\tilde{X}_p$. The basis functions provided below assume a regular background grid aligned with the Cartesian coordinates (four noded quadrilaterals in two-dimensions and eight noded hexahedra in three-dimensions). The functions are presented in one-dimension, the extension to 2D or 3D being obtained through the product of the shape functions in each direction. The one-dimensional gradients of the basis functions are obtained through

$$\nabla_{\tilde{X}}S_{vp} = \frac{1}{V_p^n}\int_{\Omega_p}\chi_p\nabla_{\tilde{X}}N_v(\tilde{X}_p)dx.\tag{25}$$
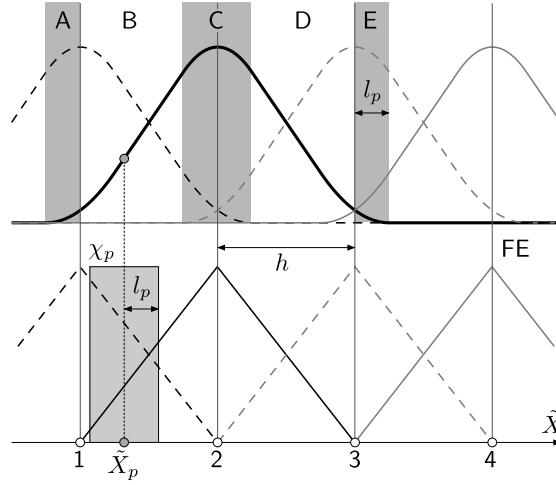
2.4.1. Standard interpolation

The basis functions for the standard material point method are obtained by replacing the characteristic function, χ_p, with a Dirac delta function, giving

$$\begin{aligned} S_{vp} &= 1 + (\tilde{X}_p - \tilde{X}_v)/h & -h &< \tilde{X}_p - \tilde{X}_v \leq 0\\ S_{vp} &= 1 - (\tilde{X}_p - \tilde{X}_v)/h & 0 &< \tilde{X}_p - \tilde{X}_v \leq h, \end{aligned}\tag{26}$$

where h is the size of the background grid (distance between the nodes in each direction) and $\tilde{X}_v$ is the position of the node (or vertex) associated with the basis function. The gradients of the basis functions with respect to the material point position at the start of the loadstep are

$$\begin{aligned} \nabla_{\tilde{X}}S_{vp} &= 1/h & -h &< \tilde{X}_p - \tilde{X}_v \leq 0\\ \nabla_{\tilde{X}}S_{vp} &= -1/h & 0 &< \tilde{X}_p - \tilde{X}_v \leq h. \end{aligned}\tag{27}$$

---

[2] Note that in domain-based material point methods (GIMP, CPDI1, CPDI2) it is possible to specify surface tractions on the outer boundaries of the material point domains.

Fig. 1. Generalised interpolation basis functions (top) and standard finite element (FE) shape functions (bottom), where the numbers are associated with the grid nodes and the letters with the different conditions in (28).

2.4.2. Generalised interpolation

The particular form of the generalised interpolation material point method adopted in this paper assumes a unity hat function of length $2l_p$ centred on $\tilde{X}_p$ as the characteristic function. This results in the following basis functions

$$
\begin{aligned}
\mathsf{A}: \quad & S_{vp} = \frac{(h + l_p + \tilde{X}_p - \tilde{X}_v)^2}{4hl_p} & -h - l_p &< \tilde{X}_p - \tilde{X}_v \le -h + l_p \\
\mathsf{B}: \quad & S_{vp} = 1 + \frac{\tilde{X}_p - \tilde{X}_v}{h} & -h + l_p &< \tilde{X}_p - \tilde{X}_v \le -l_p \\
\mathsf{C}: \quad & S_{vp} = 1 - \frac{(\tilde{X}_p - \tilde{X}_v)^2 + l_p^2}{2hl_p} & -l_p &< \tilde{X}_p - \tilde{X}_v \le l_p \\
\mathsf{D}: \quad & S_{vp} = 1 - \frac{\tilde{X}_p - \tilde{X}_v}{h} & l_p &< \tilde{X}_p - \tilde{X}_v \le h - l_p \\
\mathsf{E}: \quad & S_{vp} = \frac{(h + l_p - \tilde{X}_p + \tilde{X}_v)^2}{4hl_p} & h - l_p &< \tilde{X}_p - \tilde{X}_v \le h + l_p.
\end{aligned}
\tag{28}
$$

These one-dimensional generalised interpolation basis functions are shown in Fig. 1 for node 2 where the A through E regions correspond to the five conditions in (28). In regions B and D, the generalised interpolation functions are the same as the conventional finite element functions, as the material point's influence domain lies entirely within the finite element. The basis functions in regions A, C and E (grey regions in the top figure) depart from the conventional finite element functions due to the material point domain overlapping multiple elements. The one-dimensional gradients of the basis functions with respect to the material point position at the start of the loadstep are

$$
\begin{aligned}
& \nabla_{\tilde{X}} S_{vp} = \frac{(h + l_p + \tilde{X}_p - \tilde{X}_v)}{2hl_p} & -h - l_p &< \tilde{X}_p - \tilde{X}_v \le -h + l_p \\
& \nabla_{\tilde{X}} S_{vp} = 1/h & -h + l_p &< \tilde{X}_p - \tilde{X}_v \le -l_p \\
& \nabla_{\tilde{X}} S_{vp} = -\frac{(\tilde{X}_p - \tilde{X}_v)}{hl_p} & -l_p &< \tilde{X}_p - \tilde{X}_v \le l_p \\
& \nabla_{\tilde{X}} S_{vp} = -1/h & l_p &< \tilde{X}_p - \tilde{X}_v \le h - l_p \\
& \nabla_{\tilde{X}} S_{vp} = -\frac{(h + l_p - \tilde{X}_p + \tilde{X}_v)}{2hl_p} & h - l_p &< \tilde{X}_p - \tilde{X}_v \le h + l_p.
\end{aligned}
\tag{29}
$$

As with the basis functions in (28), when a material point's domain lies entirely within a finite element the gradient of the basis functions equals that of the standard finite element functions.

2.5. Material point & domain updating

At the end of each loadstep the material point positions, volumes and (if appropriate) domain half-lengths, l_p, should be updated. The updated positions of the material points at the end of the loadstep are given by

$$(x_p)_i = (\tilde{X}_p)_i + \underbrace{\sum_{v=1}^{n} (S_{vp})(\Delta u_i)_v}_{(\Delta u_p)_i}, \tag{30}$$

where $(\Delta u_p)_i$ is the displacement of the material point over the loadstep. The volumes of the material points are updated according to (19).

In generalised interpolation methods it is necessary to update the size of the material point influence domains (which then control the volume associated with the material point). Previously it has been proposed to use the deformation gradient for this update, however problems arise when the rotational component of the deformation gradient is non-zero.[3] Following the approach of Charlton et al. [19], the domain half-lengths, l_p, are updated according to the symmetric material stretch, U_{ij}, defined as

$$U_{ij} = \sqrt{F_{ki} F_{kj}} \qquad \text{where} \qquad F_{ij} = R_{ik} U_{kj} \tag{31}$$

and R_{ij} is the rotational component of the deformation gradient. It should be clear from the above equation that the material stretch tensor is equivalent to the deformation gradient rotated back into the original reference coordinates. The material point domains are updated according to

$$(l_p)_i = (l_{p_0})_i U_{ii}, \tag{32}$$

where no summation is implied on the repeated index; U_{ii} simply indicates the diagonal components of U_{ij}.

2.6. Computational procedure

In the previous sub-section an implicit quasi-static large deformation elasto-plastic formulation of the material point method has been described. The steps in the implemented algorithm are concisely summarised below.

The applied body forces and/or tractions are split into a number of loadsteps and for each of these steps the following process is adopted:

1. calculate the stiffness contribution, $[k^p]$, of all of the material points using (18) and assemble the individual contribution of each material point into the global stiffness matrix, $[K]$;
2. calculate the internal force contribution, $\{f^p\}$, of all of the material points using (20) and assemble the contributions into the global internal force vector, $\{f^R\}$, in (12);
3. increment the external tractions and/or body forces in (12) and solve for the nodal displacements within a loadstep, using the N–R process (13) until the out-of-balance force converges within a specified tolerance;
4. the material point positions, volumes and domain lengths can then be updated through interpolation from the incremental nodal displacements, deformation gradient and stretch tensor using (30), (19) and (32); and
5. reset or replace the background grid.

In this paper we reset the background grid after each loadstep to the original regular background grid. However, at step 5 the grid can be replaced by a completely new grid if required.

3. Volumetric locking

Fully integrated finite element methods for stress analysis suffer from volumetric locking when the constitutive behaviour of the integration points is near-incompressible (isochoric flow plasticity, for example) leading to an over-stiff response. For higher-order finite elements one way to mitigate this issue is to use reduced integration, however

---

[3] Essentially material point domains spuriously vanish with large rotational deformation; see [19] and the numerical examples contained within for a detailed explanation.

it is not possible to adopt this approach for linear quadrilateral and hexahedral elements without introducing spurious energy modes (such as hour-glassing). Material point methods usually adopt these low order elements and suffer from severe volumetric locking due to the low order of basis of the background grid combined with the higher numbers of material points required to ensure sufficient accuracy of the stiffness integration due to their non-optimum placement (compared to a Gauss quadrature rule, for example).

One method for overcoming volumetric locking in low-order finite elements is the $\bar{F}$ approach of de Souza Neto et al. [12], where the volumetric and deviatoric components of the deformation gradient are sampled at different locations. The deformation gradient becomes

$$\bar{F}_{ij} = \left(\frac{\det(F_{ij}^0)}{\det(F_{ij})} \right)^{1/n_D} F_{ij}, \tag{33}$$

where n_D is the number of physical dimensions and F_{ij}^0 is the deformation gradient obtained from the deformation field at the centre of the element. Therefore the volumetric component of the deformation gradient for all of the Gauss points within an element is obtained from a single point and this relaxes the volumetric constraint on the element when the material behaviour is near incompressible. However, the location of the volumetric sampling point is rather arbitrary and is not restricted to be at the centre of the element [15], what is essential is to reduce the volumetric constraint on the element in order to mitigate volumetric locking. This approach appears to be similar to the concept of selective reduced integration where the shear and/or volumetric strains are evaluated at the mid point of the element through appropriate modification of the strain–displacement matrix. In the case of an element with a linear basis, the centre is the obvious location for the volumetric sampling point as this corresponds to the location of a single point Gauss quadrature scheme which is an order lower than the standard 2 point per local direction scheme used to integrate the element. In material point methods the hierarchical numerical integration structure is lost and therefore the appropriate location for the volumetric sampling point is less obvious. Despite the perceived similarity with selective reduced integration, in the same way that the $\bar{F}$ approach cannot be seen as a geometrically non-linear extension to $\bar{B}$ methods [7], the $\bar{F}$ approach is fundamentally different to selective reduced integration. In particular, selective reduced integration and $\bar{B}$ methods directly modify the strain–displacement matrix (effectively modifying the strain energy function), and use this revised strain–displacement matrix in the calculation of the internal force and stiffness of the elements. In the $\bar{F}$ approach the calculation of the deformation gradient is modified (changing the stress constitutive function) and the appropriate spatial tangent formulated due to this change. See Section 15.1 of [15] for a detailed discussion of this point. Despite their technical differences, all of the approaches share the common goal of reducing the volumetric constraint placed on an element and avoiding locking.

In this paper we adopt the $\bar{F}$ approach [12] to mitigate the issue of volumetric locking and make it applicable to both standard and generalised interpolation material point methods. The $\bar{F}$ approach has been adopted for the following reasons:

1. it does not introduce any additional unknowns into the linear system;
2. it is straightforward to implement within existing material point formulations;
3. it does not place any restriction on the choice of constitutive model;
4. it does not introduce any tuning parameters into the code; and
5. it does not introduce any additional material points to track the volumetric behaviour.

3.1. Deformation gradient

Here we adopt the incremental equivalent of (33), giving the $\bar{F}$ deformation gradient increment as

$$\Delta\bar{F}_{ij} = \left(\frac{\det(\Delta F_{ij}^0)}{\det(\Delta F_{ij})} \right)^{1/n_D} \Delta F_{ij}, \tag{34}$$

where ΔF_{ij}^0 is the volumetric component of the deformation gradient increment. It is straightforward to modify the standard material point method by replacing ΔF_{ij} with $\Delta\bar{F}_{ij}$ in the finite deformation formulation presented in Section 2.1. This is because the shape functions are directly adopted from the finite element basis. However, it is

more appropriate to use the geometric centre of the material points located within a given finite element rather than the centre of the element. This is due to two key reasons:

1. when a single material point is used to integrate the background grid cell the $\bar{F}$ deformation gradient, (34), equals the standard deformation gradient; and
2. when a background grid cell is only partially filled with material points the volumetric behaviour is centred on the physical region.

The increment in the deformation gradient used to approximate the volumetric behaviour can be obtained from (21) with the derivatives of S_{vp} evaluated at the appropriate position within the background element.

3.2. $\bar{F}$ for generalised MPMs

While extending the standard MPM to a $\bar{F}$ formulation is straightforward, the extension of generalised interpolation material point methods to overcome volumetric locking is less obvious. The basic concept is that, consistent with the $\bar{F}$ approach [12], the volumetric behaviour of each background grid cell is spatially constant and controlled by the basis functions (and derivatives) at the centre of the element. The shape functions of a generalised interpolation point are then obtained through the convolution of these basis functions with the particle characteristic function as in the standard generalised interpolation method. However, this does not imply that the material points contributing to each element have the same volumetric behaviour as each point is influenced by the elements which they overlap. Essentially the volumetric behaviour of a generalised interpolation material point will be dictated by a domain-overlap weighted contribution from the background elements.

Assuming that the element basis functions take the value at the centre of the element ($N_i = 1/2$ for linear elements in one dimension) across the entire element and that the characteristic function, χ_p, remains a unity hat function of width $2l_p$, the one-dimensional generalised interpolation shape functions become

$$S_{vp}^0 = \frac{1}{V_p^n} \int_{\Omega_p} \frac{1}{2} \, dx, \tag{35}$$

which gives three conditions

$$
\begin{array}{llll}
\text{A}: & S_{vp}^0 = (h + l_p + \tilde{X}_p - \tilde{X}_v)/4l_p & -h - l_p < \tilde{X}_p - \tilde{X}_v \leq -h + l_p \\
\text{B}: & S_{vp}^0 = 1/2 & -h + l_p < \tilde{X}_p - \tilde{X}_v \leq h - l_p \\
\text{C}: & S_{vp}^0 = (h + l_p - \tilde{X}_p + \tilde{X}_v)/4l_p & h - l_p < \tilde{X}_p - \tilde{X}_v \leq h + l_p.
\end{array}
\tag{36}
$$

These basis functions are shown in Fig. 2 along with the corresponding finite element functions. Conditions A and C (grey regions in Fig. 2) apply where the material point's domain partially overlaps the non-zero basis function region, whereas B applies when the material point's domain fully overlaps the non-zero basis.

The one dimensional derivatives of the generalised interpolation shape functions are unchanged as they are already constant within each background element. The derivatives in multiple dimensions come from the product of (36) with the conventional derivatives (29), for example in two-dimensions

$$\frac{\partial S_{vp}^0(\tilde{X}, \tilde{Y})}{\partial \tilde{X}} = \frac{\partial S_{vp}(\tilde{X})}{\partial \tilde{X}} S_{vp}^0(\tilde{Y}). \tag{37}$$

Note that when constructing the spatial derivatives of the modified basis functions it is essential to use ΔF_{ij}^0 to map (36) into the spatial frame, that is

$$\frac{\partial(S_{vp}^0)}{\partial x_j} = \frac{\partial(S_{vp}^0)}{\partial \tilde{X}_i} \left(\Delta F_{ij}^0 \right)^{-1}. \tag{38}$$

3.3. Linearisation: modified stiffness

Modifying the volumetric component of the deformation gradient results in an additional term in the stiffness contribution of each material point to the background grid. The $\bar{F}$ stiffness of a material point for three-dimensional
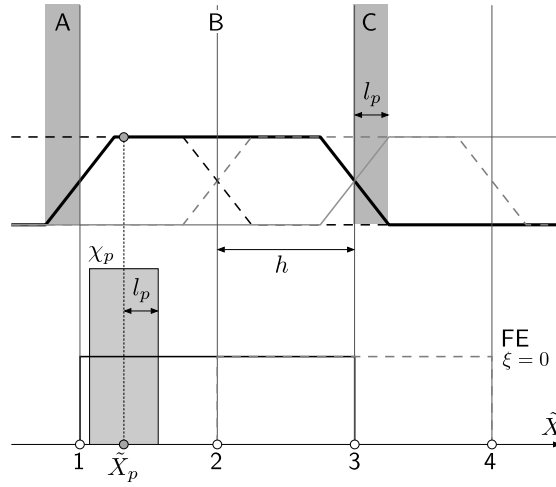
Fig. 2. $\bar{F}$ generalised interpolation basis functions (top) and shape functions sampled at the centre of the element (bottom), where the numbers are associated with the grid nodes and the letters with the different conditions in (36).

analysis becomes

$$[\bar{k}_p] = [k_p] + [G]^T \left(\frac{1}{3}\Big\{[A]\{1\} - 2\{\sigma\}\Big\}\{1\}^T\right)\Big([G_0] - [G]\Big)V_p, \tag{39}$$

where $[k_p]$ is given by (18), $[G_0]$ is the tensorial strain–displacement matrix associated with the volumetric component of the deformation gradient increment, ΔF_{ij}^0, and $\{1\} = \{1 \quad 1 \quad 1 \quad 0 \quad 0 \quad 0 \quad 0 \quad 0 \quad 0\}^T$ is a 9 by 1 vector form of δ_{ij}. For two-dimensional plane strain analysis the stiffness of a material point is

$$[\bar{k}_p] = [k_p] + [G]^T \left(\frac{1}{2}\Big\{[A]\{1\} - \{\sigma\}\Big\}\{1\}^T\right)\Big([G_0] - [G]\Big)V_p, \tag{40}$$

where $\{1\} = \{1 \quad 1 \quad 0 \quad 0\}^T$. The remainder of the material point method remains unchanged.

Note that V_p, the current volume associated with the material points is the equivalent to $\det(\partial x_i/\partial \xi_j)w_i$ in conventional finite element methods where w_i is the weight (or local volume) associated with the integration point, ξ_i are the local coordinates and $\partial x_i/\partial \xi_j$ is the Jacobian. This Jacobian is obtained at the integration point position using the basis function gradients at that location and is not modified by the $\bar{F}$ approach. Therefore, the volume used in the stiffness calculation should be obtained from (19) using the original increment in the deformation gradient, ΔF_{ij}, not the $\bar{F}$ modified increment, $\Delta \bar{F}_{ij}$.

4. Numerical examples

This section presents five numerical examples to demonstrate the performance of the proposed material point formulations. All cases adopt a linear-elastic perfectly-plastic associated flow von Mises model (also known as Prandtl–Reuss) with the following yield surface

$$f = \rho - \rho_y = 0, \tag{41}$$

where ρ_y is the yield strength of the material and $\rho = \sqrt{2J_2}$ where $J_2 = \frac{1}{2}(s_{ij}s_{ji})$ and $s_{ij} = \sigma_{ij} - \sigma_{kk}\delta_{ij}/3$.

In this paper we adopt the exact stress integration approach of Wei et al. [30][4] which includes the derivation of the algorithmically consistent tangent, $[D^{alg}]$, to ensure the correct order of convergence of the global Newton–Raphson process. Although exact stress integration routines are generally considered to be too computationally expensive for routine numerical analysis [32], the stress integration routine removes the errors associated with the stress updating process allowing better quantification of the errors associated with the boundary value solver.

---

[4] Note that exact stress integration on the Prandtl–Reuss model was first formulated by Krieg and Krieg [31], in this paper we adopt the approach of Wei et al. [30] as they were the first to linearise the algorithm to obtain the consistent tangent matrix.
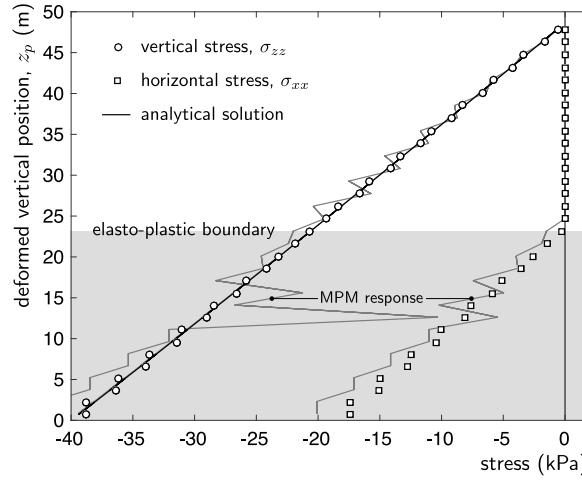
Fig. 3. Compression under self weight: stress versus vertical position for 2^4 elements and 4 material points per element.

4.1. Compression under self weight

The first example is an elasto-plastic column compressed under its own weight. The column had a height of $l_0 = 50$ m and a width of 2 m and was analysed with a plane strain assumption in the third direction. The base of the column was restrained vertically and both sides of the column were restrained in the horizontal direction. The column had a Young's modulus of 1 MPa and Poisson's ratio of 0, the yield strength of the material was set to 20 kPa and an initial density of $\varrho_0 = 80$ kg/m^3. The body force of -800 N/m^3 was applied in the vertical (Z, z) direction over 50 equal loadsteps.

The analytical solution for the vertical Cauchy stress is

$$\sigma_{zz} = \varrho_0 g(l_0 - Z), \tag{42}$$

where g is the gravitational acceleration (taken to be 10 m/s^2), l_0 is the initial height of the column and Z is the initial vertical position within the column. If Poisson's ratio is zero the stress in the horizontal directions is equal to zero when the behaviour is elastic. Once the material yields, the Cauchy stress in the horizontal direction is given by

$$\sigma_{xx} = \sigma_{yy} = \frac{1}{F_{zz}} E \ln(F_{xx}^{\mathrm{e}}), \tag{43}$$

where the vertical deformation gradient, F_{zz}, and the elastic component of the deformation gradient in the horizontal direction, F_{xx}^{e}, can be obtained using the method presented in Charlton et al. [19].

Fig. 3 shows the stress versus deformed vertical position response for the $\bar{F}$ generalised interpolation material point method where the analysis was conducted on a background grid with 16 elements in the vertical direction and 4 material points per initial background grid element. The numerical result (discrete points) shows good agreement with the analytical solution (solid black line) for both the vertical and horizontal stresses. The material points undergoing elasto-plastic behaviour are identified by the non-zero horizontal stress and the grey shaded region. The response for the $\bar{F}$ standard material point method with the same discretisation is also given (solid grey line), which demonstrates the spurious stress oscillations caused by cell-crossing instabilities in the standard material point method. Fig. 3 only shows the $\bar{F}$ responses of the standard and generalised interpolation material point methods. However, as this problem does not exhibit volumetric locking, it is not possible to distinguish between the non-$\bar{F}$ and the $\bar{F}$ formulations on this figure and therefore the non-$\bar{F}$ results have been omitted.

The convergence of the $\bar{F}$ generalised interpolation method is shown in Fig. 4, where the dimensionless error is defined as

$$\text{error} = \sum_{p=1}^{n_p} \frac{\|(\sigma_p)_{zz} - \sigma_{zz}^a(Z_p)\| V_p^0}{(\rho_0 g l_0) V_0}, \tag{44}$$
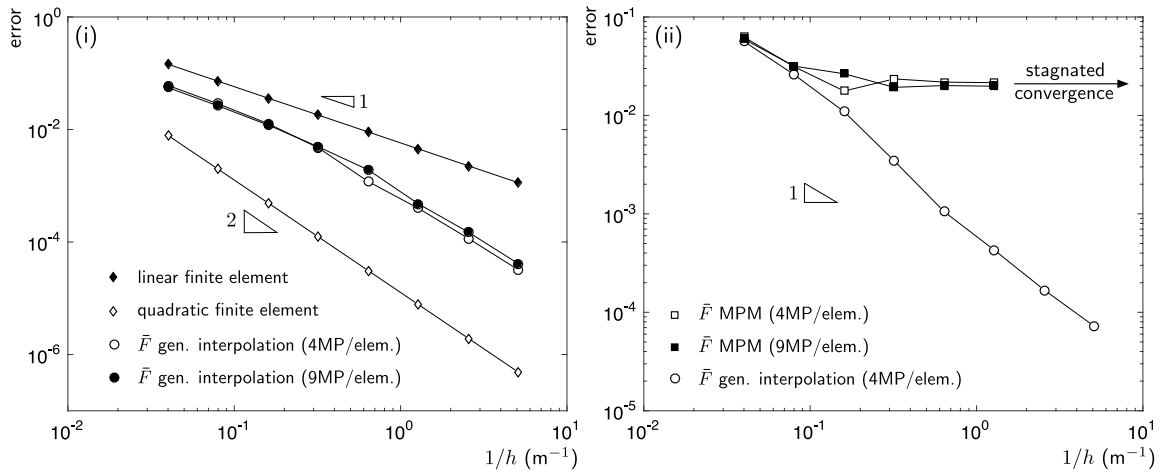
Fig. 4. Compression under self weight: convergence of the $\bar{F}$ generalised interpolation formulation for (i) elastic and (ii) elasto-plastic material behaviour.

where $\|(\cdot)\|$ is the L_2 norm of $(\cdot)$, n_p is the total number of material points, $(\sigma_p)_{zz}$ is the Cauchy stress in the vertical direction at a material point, Z_p is the material point's original position, V_p^0 is the original volume associated with the material point and σ_{zz}^a is the analytical stress solution in the vertical direction, given by (42). The denominator of (44) is the product of the vertical stress at the base of the column multiplied by the column's original volume, V_0.

Fig. 4(i) shows the convergence behaviour of the $\bar{F}$ generalised interpolation material point method under purely elastic behaviour (same material parameters and loading as above but with $\rho_y = \infty$) compared to that of fully-integrated bi-linear 4 noded and bi-quadratic 8 noded quadrilateral elements. As reported by Charlton et al. [19], the error and convergence rate of the $\bar{F}$ generalised interpolation material point method lies between that of linear and quadratic finite elements. This is due to the basis functions being linear or quadratic depending if the material point is fully contained within a single element or spanning between multiple elements (see Eq. (28)). There is little difference seen in the convergence rates of the $\bar{F}$ generalised interpolation approach with 4 or 9 material points per initial background grid cell.

Fig. 4(ii) shows the convergence behaviour of the $\bar{F}$ standard and generalised interpolation material point methods with elasto-plastic material behaviour. Although the standard material point method converges for low numbers of elements, as the number of elements in the vertical direction exceeds 8 ($h = 6.25$ m) the convergence stagnates due to cell-crossing errors. This error is reduced by the generalised interpolation material point method which continues to converge at a rate between linear and quadratic finite elements; the average convergence rate over the four finest discretisations is approximately 1.3. As before, Fig. 4 only shows the $\bar{F}$ convergence behaviour of the standard and generalised interpolation material point methods. As this problem does not exhibit volumetric locking, the convergence behaviour of the non-$\bar{F}$ formulations are the same as their $\bar{F}$ counterparts in this case. Volumetric locking is not observed in this problem due to the simplicity of the deformation field. The deformation in each background grid cell is zero in the x and y directions and linear or quadratic in the z direction for the standard and generalised interpolation material point methods, respectively. The simplicity of this deformation field allows the standard formulations to capture the volumetric behaviour without locking, with the background grid nodes deforming in the vertical direction corresponding to the volumetric behaviour of their associated material points. This is not the case for the other numerical examples that follow.

4.2. Double notched plate

The second example is the analysis of the plane strain stretching of a double-notched plate. The problem was initially presented by Nagtegaal et al. [33] for small strain plasticity to demonstrate the spurious response of standard finite elements and was subsequently re-analysed in a number of papers [8,12,34]. In this analysis the plate had a Young's modulus of 206.9 GPa, Poisson's ratio of 0.29 and a yield stress of $\rho_y = 0.45$ GPa. Nagtegaal et al. [33]
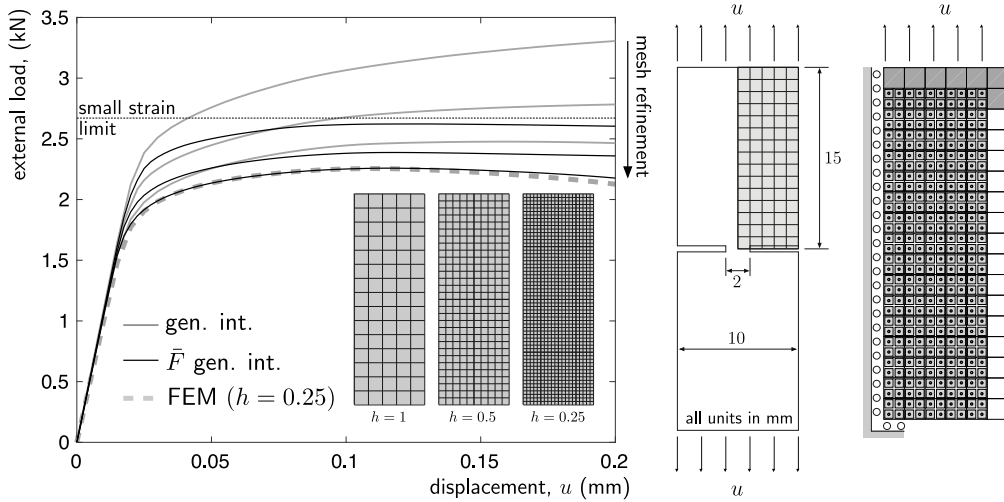
Fig. 5. Double notched plate: force displacement response for the generalised interpolation material point method with three different background grids.

provided the small strain analytical limit load, controlled by the stress at the notch $\sigma_{\text{lim}} \approx 2.97\sigma_y$. The specimen had a total height and width of 30 mm and 10 mm respectively, with a 2 mm unit linking ligament at mid height. For this geometry the small strain limit load is $F_{\text{lim}} \approx 2.673$ kN.

In the numerical analysis, due to symmetry only one quarter of the specimen was discretised, as shown in the middle figure of Fig. 5. A displacement of 0.2 mm was applied in 80 equal displacement-controlled increments. The material points for the generalised interpolation method with 4 material points per element are shown on the background grid to the right of Fig. 5. Roller boundary conditions were applied to the left edge of the domain and the first 1 mm of the base of the background grid. To impose the prescribed displacement on the top of the specimen the background mesh was extended by 2 mm at the top of the sample (shown by the dark grey shaded region) and a rigid body vertical displacement imposed on this region. The physical domain was also extended by 1 mm into this region.

Fig. 5 shows the force versus displacement response of both the standard generalised interpolation (grey lines) and $\bar{F}$ generalised interpolation (black lines) material point methods for three different discretisations ($h = 1$ mm, $h = 0.5$ mm and $h = 0.25$ mm). In all cases the standard generalised interpolation method predicts an over-stiff response due to volumetric locking induced by the isochoric flow rule. This is particularly evident for the $h = 1$ mm and $h = 0.5$ mm meshes where a limit load is not reached. The $\bar{F}$ approach removes this volumetric locking behaviour and the resulting material point method response under predicts the small strain limit load of [33] due to the finite deformation mechanics accounting for the necking of the linking ligament. A four noded quadrilateral $\bar{F}$ finite element response with $h = 0.25$ mm is also shown in Fig. 5 (thick grey dashed line) which agrees well with the $\bar{F}$ generalised interpolation response; 0.14% difference in the peak force.

Fig. 6 shows the force versus displacement response for $h = 1$ mm for (i) generalised interpolation and (ii) standard material point methods with different numbers of material points per element in the initial discretisation. In Fig. 6(i) all of the conventional generalised interpolation responses over-predict the external force and, as expected, the external force increases as the number of material points is increased due to increasing the number of constraints placed on the volumetric behaviour of the elements. The $\bar{F}$ generalised interpolation force versus displacement responses are very similar for 4, 9 and 16 material points per element. The force does increase slightly as increasing the number of material points reduces the integration errors associated with the numerical approximation of the internal force. As before, the $\bar{F}$ generalised interpolation response agrees well with the finite element response (thick dashed grey line) and all of the responses are below the small strain limit load. The two inset figures show the $\bar{F}$ deformed material points at the end of the analysis for 4 and 16 material points per element. The generalised interpolation domains have been scaled by 0.8 for clarity between adjacent points.

Fig. 6(ii) gives the force versus displacement response of the standard material point (grey lines) and the $\bar{F}$ material point (black lines) methods. For a single material point per element both simulations under-predict the limit load and
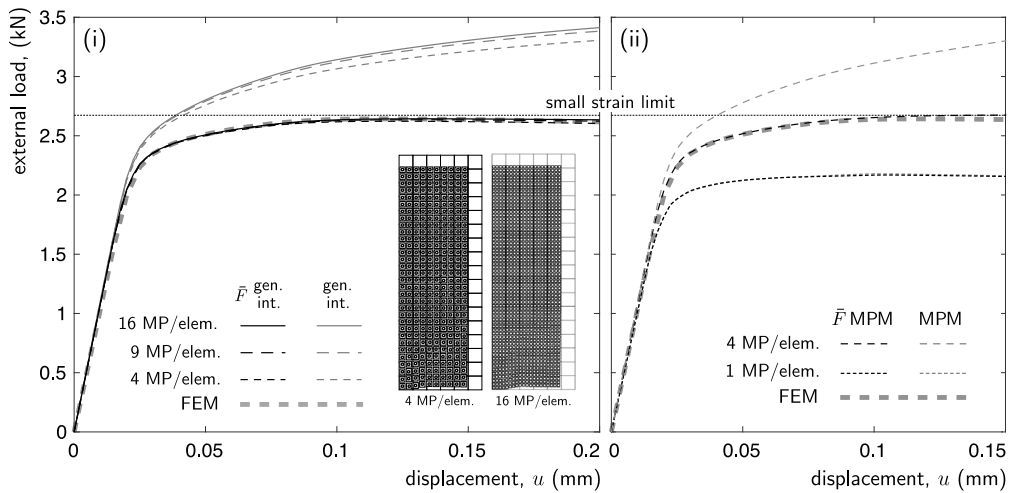
Fig. 6. Double notched plate: force displacement response with $h = 1$mm and different numbers of material points per element for: (i) generalised interpolation and (ii) standard material point methods (where the displacement has been truncated for clarity).

Table 1
Double notched plate convergence: normalised out of balance force for $\bar{F}$ generalised interpolation with $h = 1$ mm and 4 material points per element for loadsteps 76 through 80.

| NRit	Loadstep				
	76	77	78	79	80
1	5.231×10^{-02}	5.728×10^{-02}	5.226×10^{-02}	5.844×10^{-02}	5.294×10^{-02}
2	4.388×10^{-03}	6.177×10^{-03}	6.090×10^{-03}	6.345×10^{-03}	5.725×10^{-03}
3	6.653×10^{-05}	6.404×10^{-04}	4.501×10^{-04}	3.582×10^{-04}	3.801×10^{-04}
4	2.173×10^{-09}	2.286×10^{-05}	5.175×10^{-05}	7.387×10^{-06}	2.022×10^{-07}
5	–	1.513×10^{-10}	1.795×10^{-09}	1.596×10^{-11}	–

are very similar in their overall response. As the number of material points per element is increased to 4, volumetric locking is observed in the standard material point method whereas the $\bar{F}$ approach reaches a limit load similar to that of the finite element method (shown by the thick grey dashed line). Note that the standard material point method provides a reasonable response in this case due to the relatively small displacements in the problem.

The convergence rate of the $\bar{F}$ generalised interpolation approach is demonstrated in Table 1 with $h = 1$ mm and 4 material points per initial background grid element for loadsteps 76 through 80. The tolerance on the normalised out of balance force was set to 1×10^{-6}, where the residual L_2 norm was normalised by the L_2 norm of the external reactions. It is clear from the table that the algorithm achieves an asymptotic quadratic convergence rate, with the final iteration in each loadstep being at (or near quadratic), thereby confirming the correct implementation of the generalised interpolation $\bar{F}$ method.

4.3. Elasto-plastic collapse

The next analysis presented in this paper is the collapse of a 16 m by 8 m plane strain block under self weight. A background grid with $h = 1$ m in two directions was adopted and the domain was discretised by 9 material points per initial background grid element ($l_p^0 = \frac{1}{3}$ m in both directions). Due to symmetry only half of the body was modelled and roller boundary conditions were imposed directly on the background mesh on the base and the line of symmetry (see Fig. 7). The body had a Young's modulus of 100 kPa, Poisson's ratio of 0.3 and a yield stress of $\sigma_y = 15$ kPa and was subjected to a body force of -625 N/m^3 over 20 equal loadsteps. Although there is no analytical solution for this problem, it serves as a useful demonstration of the ability of the proposed formulation to be used for the type of very large deformation problems to which material point methods are typically applied.
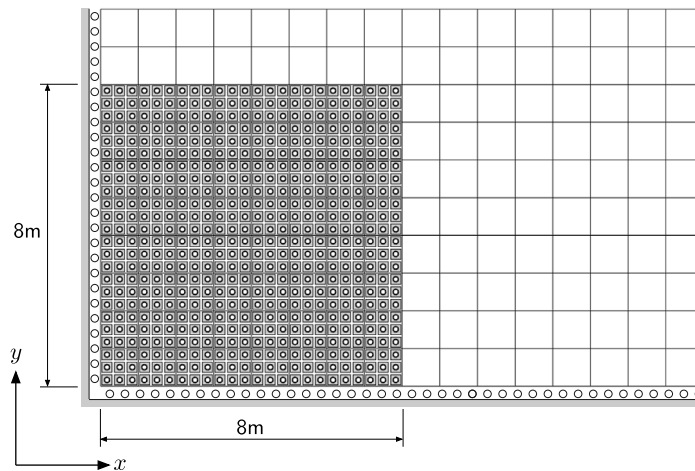
Fig. 7. 2D collapse: problem definition and initial discretisation.

Fig. 8 shows final positions of the material point domains for both the standard and $\bar{F}$ generalised interpolation methods. The $\bar{F}$ method also experiences slightly higher displacements, particularly on the top surface of the deforming body. The domains have been coloured according to the material points' vertical, σ_{yy} (top), and horizontal, σ_{xx} (middle), stresses. The $\bar{F}$ method reduces the stress oscillations seen in the standard material point method by relaxing the volumetric constraint on the deformation of the background finite elements. This is most evident in the plot of the hydrostatic stress, $p = \sigma_{ii}/3$, at the bottom of Fig. 8, where the spurious stress oscillations are removed by the $\bar{F}$ approach. The susceptibility of material point methods to spurious stress oscillations is more clearly shown in the next section.

4.4. Plane strain localisation

The penultimate analysis presented in this paper is the plane strain localisation of a body of half-width 6.413 mm and half-height of 26.667 mm. The body was discretised using 1600 generalised interpolation material points (16 MPs per background grid cell) and the background elements were arranged in a regular grid with lengths in the x and y directions of 1.283 mm and 1.333 mm, respectively. The initial layout of the material points and the background grid are shown in Fig. 9(i). The material had a Young's modulus of 41.3 GPa and a Poisson's ratio of 0.29 and a von Mises yield strength of $\rho_y = 0.45$ GPa. In order to trigger the localisation, 16 material points within the outermost mid height element had their yield strengths reduced by 10% (as shown by the dark grey shaded region in Fig. 9(i)). The top edge of the specimen was subjected to a displacement of 0.64 mm over 10 loadsteps via direct imposition of the displacements on the background grid.

Fig. 9(ii) and (iii) show the vertical, σ_{yy}, stress distribution and the deformed material point domains at the end of the analysis. Even for the small imposed deformation, the standard generalised interpolation material point method clearly shows spurious stress oscillations due to volumetric locking which are mitigated by the $\bar{F}$ approach. The stress patches seen in Fig. 9(iii) are due to the linear basis of the background finite element mesh and the stress concentration on the top right corner of the domain, highlighted by the circle A, is due to the nature of the imposed boundary condition, restricting x and specifying y motion, respectively.

4.5. Three-dimensional rigid footing

The final example presented in this paper is that of smooth square rigid footing bearing onto a weightless three-dimensional domain. Due to symmetry only a quarter of the physical problem was modelled and the footing had a half width of 0.5 m and the simulated domain was 5 m in length in each direction. The same material properties were adopted as de Souza Neto et al. [15] for their plane strain analysis of a rigid footing: Young's modulus of 10 GPa,
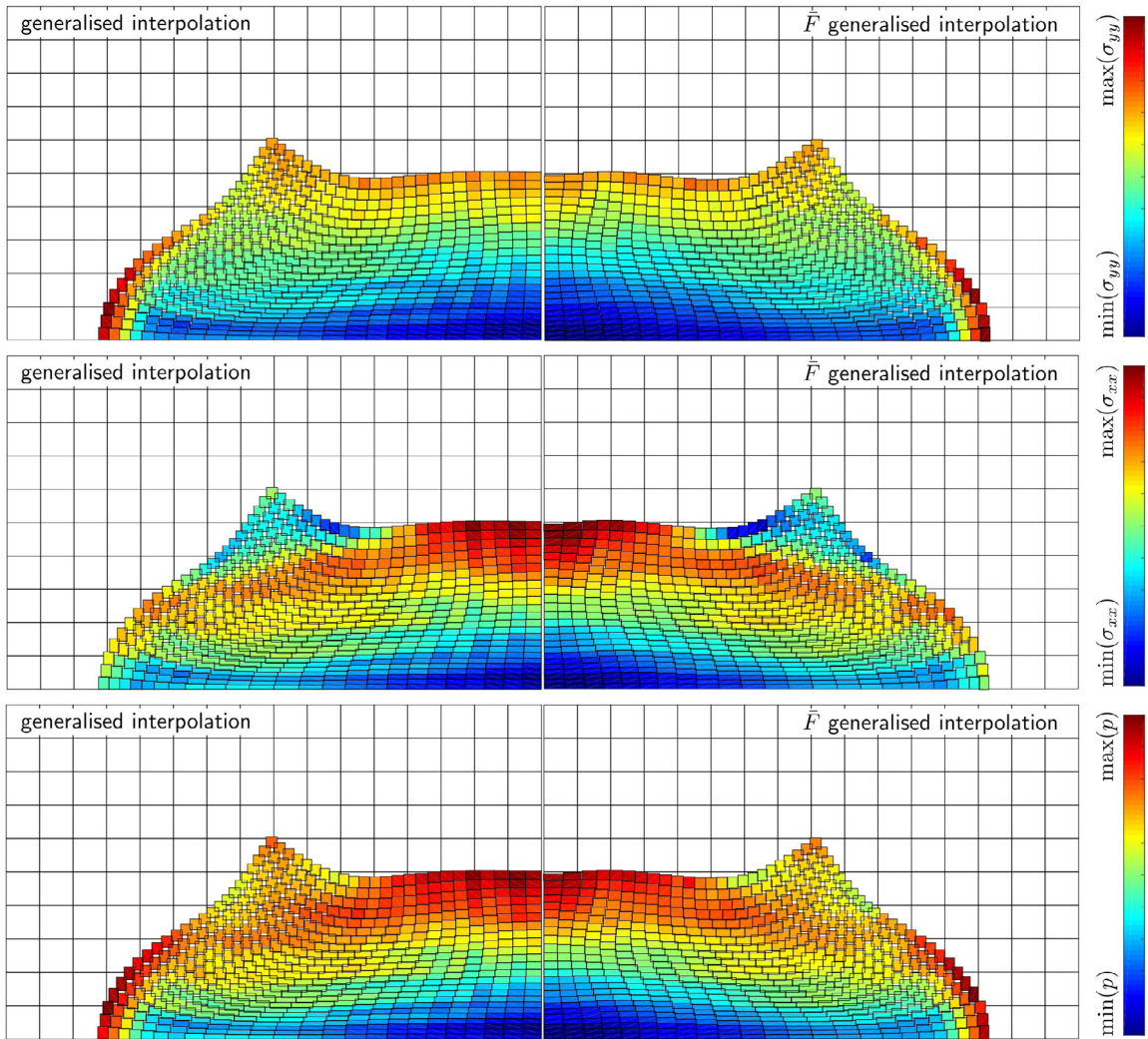
Fig. 8. 2D collapse: deformed material point domains coloured according to their vertical, σ_{yy} (top), horizontal, σ_{xx} (middle), and hydrostatic, $p = \sigma_{ii}/3$ (bottom), stresses for the standard and $\bar{F}$ generalised interpolation material point methods.

Poisson's ratio of 0.48 and von Mises yield strength of $\rho_y = 693$ kPa. The smooth footing[5] was displaced vertically (z-direction) by 0.002 m over 200 loadsteps and roller boundary conditions were imposed on the sides and the base of the domain. All of the boundary conditions were imposed using the implicit boundary method of Cortis et al. [29]. A relatively coarse regular background grid of tri-linear hexahedral elements with $h = 0.2$ m was used to analyse the problem and the physical domain was discretised using 8 standard material points per background grid cell (125,000 material points in total).
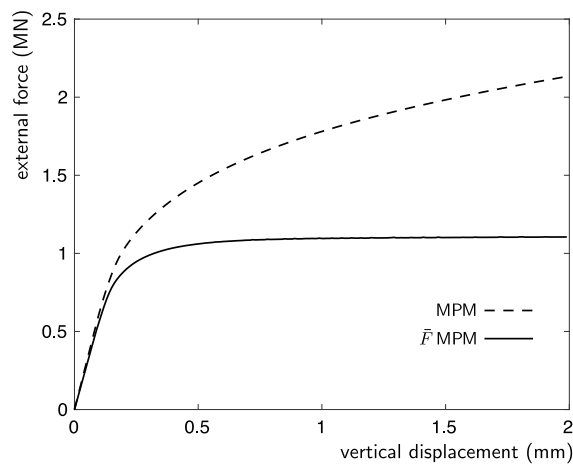
The force versus displacement response for the standard and $\bar{F}$ material point methods are shown in Fig. 10. The standard formulation locks and predicts an over-stiff response whereas the $\bar{F}$ formulation reaches limit load, as expected for this type of analysis. Due to the small imposed displacement, material points do not cross between background grid cells and both formulations give a smooth response.

The minor principal (most compressive) stress distribution at the end of the analysis for the two formulations are shown in Fig. 11. As with the previous examples, the standard material point formulation contains spurious stress

---

[5] The term "smooth" is used to denote that the material if free to translate horizontally beneath the footing, only the vertical displacement is specified.
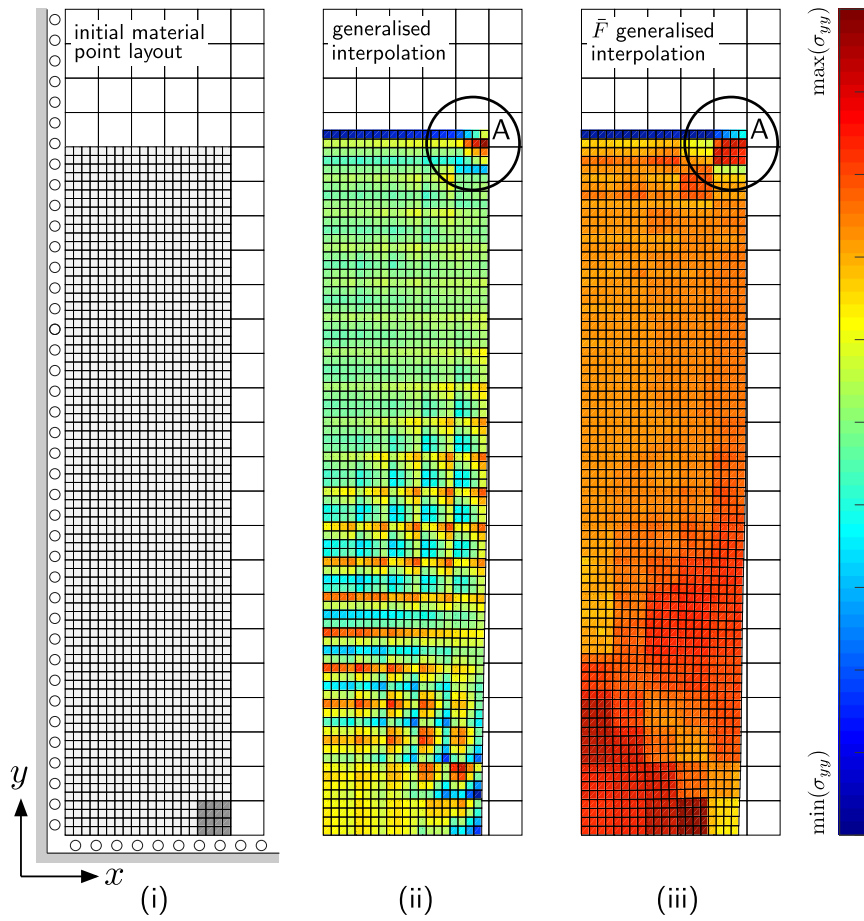
Fig. 9. 2D localisation: (i) initial discretisation and deformed material point positions shaded according to their vertical stress for: (ii) generalised interpolation and (iii) $\bar{F}$ generalised interpolation formulations.

Fig. 10. 3D footing: force displacement response for standard and $\bar{F}$ MPMs.
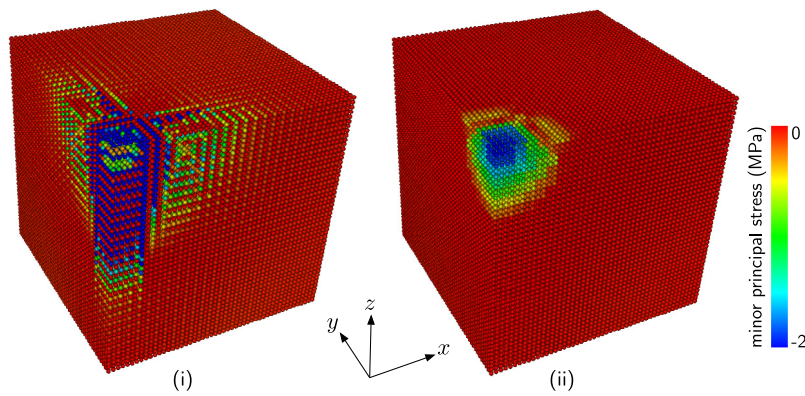
Fig. 11. 3D footing: minor principal stress for (i) standard and (ii) $\bar{F}$ MPMs. (For interpretation of the references to colour in this figure legend, the reader is referred to the web version of this article.)

oscillations caused by volumetric locking. In particular, the column of material points underneath the footing oscillate between tensile and compressive stress states. The $\bar{F}$ formulation stress distribution shown in Fig. 11(ii) demonstrates the correct compressive region underneath the footing, as shown by the blue-shaded particles.

5. Conclusions

Material point methods typically use a low order background grid for numerical computation with high numbers of material points per grid cell to combat the errors induced by non-optimum placement of integration points. Combining this with near-incompressible material behaviour (such as isochoric flow plasticity models) leads to severe volumetric locking and an over-stiff global response.

This paper has presented for the first time a general method to overcome volumetric locking in both standard and generalised interpolation material point methods for near-incompressible non-linear solid mechanics. The method does not place any restriction on the form of constitutive model used and is straightforward to implement into existing implicit material point method codes.

The performance of the method has been demonstrated on a number of two and three-dimensional examples and its correct implementation confirmed through convergence studies validated against analytical solutions and obtaining the correct order of convergence within the global N–R equilibrium iterations. In particular, the proposed formulation has been shown to remove the over-stiff volumetric behaviour of conventional material point methods and reduce stress oscillations.

In the standard material point formulation the volumetric sampling point for the $\bar{F}$ approach has been taken as the geometric centre of the material points in each element rather than the centre of the background grid cell. Although the position of the volumetric sampling point will change the results, it has been found that the location of the volumetric sampling point has little influence on the global response. The key point on reducing volumetric locking in linear background grid material point methods is lowering the volumetric constraint placed on the background grid cells such that the volumetric behaviour is only sampled at a single point. For a given analysis there may be an optimum location for this volumetric sampling point, however this paper has proposed a general methodology to avoid volumetric locking whilst not introducing any special cases in the numerics.

It is straightforward to extend this approach to other material point methods. For example, in CPDI1 [35] and CPDI2 [36] the basis functions (and their derivatives) are obtained by sampling the finite element basis functions at the vertices of the material point domains and then assuming linear interpolation between these values to integrate over the domain. Here, in a similar way to the generalised interpolation approach presented in this paper, one would simply replace the standard basis functions with the value at the centre of the element. Therefore the $\bar{F}$ approach for overcoming volumetric locking presented in this paper is applicable to all material point formulations available in the current literature. It would also be possible to apply the method to other material point methods that use non-standard basis functions. For example, the mesh-grading of Lian et al. [37], which allows for hanging nodes within the material point method by modifying the finite element basis, could adopt the proposed $\bar{F}$ approach through selective volumetric sampling of the modified basis functions.

Acknowledgements

References

[1] D. Sulsky, Z. Chen, H. Schreyer, A particle method for history-dependent materials, Comput. Methods Appl. Mech. Engrg. 118 (1) (1994) 179–196.
[2] J.U. Brackbill, H.M. Ruppel, FLIP - A method for adaptively zoned, particle-in-cell calculations of fluid flows in two dimensions, J. Comput. Phys. 65 (1986) 314–343.
[3] F. Harlow, The particle-in-cell computing method for fluid dynamics, Methods Comput. Phys. 3 (319–343) (1964).
[4] M. Steffen, R.M. Kirby, M. Berzins, Analysis and reduction of quadrature errors in the material point method (MPM), Internat. J. Numer. Methods Engrg. 76 (6) (2008) 922–948.
[5] J. Simo, R. Taylor, K. Pister, Variational and projection methods for the volume constraint in finite deformation elasto-plasticity, Comput. Methods Appl. Mech. Engrg. 51 (1–3) (1985) 177–208.
[6] T. Sussman, K.-J. Bathe, A finite element formulation for nonlinear incompressible elastic and inelastic analysis, Comput. Struct. 26 (1) (1987) 357–409.
[7] B. Moran, M. Ortiz, C.F. Shih, Formulation of implicit finite element methods for multiplicative finite deformation plasticity, Internat. J. Numer. Methods Engrg. 29 (3) (1990) 483–514.
[8] J. Simo, F. Armero, Geometrically non-linear enhanced strain mixed methods and the method of incompatible modes, Internat. J. Numer. Methods Engrg. 33 (1992) 1413–1449.
[9] S. Reese, P. Wriggers, A stabilization technique to avoid hourglassing in finite elasticity, Internat. J. Numer. Methods Engrg. 48 (1) (2000) 79–109.
[10] W.A. Wall, M. Bischoff, E. Ramm, A deformation dependent stabilization technique, exemplified by EAS elements at large strains, Comput. Methods Appl. Mech. Engrg. 188 (4) (2000) 859–871.
[11] M.A. Crisfield, G.F. Moita, A co-rotational formulation for 2-d continua including incompatible modes, Internat. J. Numer. Methods Engrg. 39 (15) (1996) 2619–2633.
[12] E. de Souza Neto, D. Perić, M. Dutko, D.R.J. Owen, Design of simple low order finite elements for large strain analysis of nearly incompressible solids, Int. J. Solids Struct. 33 (1996) 3277–3296.
[13] E. de Souza Neto, F.M.A. Pires, D.R.J. Owen, F-bar-based linear triangles and tetrahedra for finite strain analysis of nearly incompressible solids. Part I: formulation and benchmarking, Internat. J. Numer. Methods Engrg. 62 (3) (2005) 353–383.
[14] S. Doll, K. Schweizerhof, R. Hauptmann, C. Freischläger, On volumetric locking of low-order solid and solid-shell elements for finite elastoviscoplastic deformations and selective reduced integration, Eng. Comput. 17 (7) (2000) 874–902.
[15] E. de Souza Neto, D. Perić, D. Owen, Computational Methods for Plasticity: Theory and Applications, John Wiley & Sons Ltd, 2008.
[16] R. de Borst, M.A. Crisfield, J.J.C. Remmers, C.V. Verhoosel, Nonlinear Finite Element Analysis of Solids and Structures, Wiley, 2012.
[17] F. Zhang, X. Zhang, K.Y. Sze, Y. Lian, Y. Liu, Incompressible material point method for free surface flow, J. Comput. Phys. 330 (2017) 92–110.
[18] C.M. Mast, P. Mackenzie-Helnwein, P. Arduino, G.R. Miller, W. Shin, Mitigating kinematic locking in the material point method, J. Comput. Phys. 231 (16) (2012) 5351–5373.
[19] T.J. Charlton, W.M. Coombs, C.E. Augarde, iGIMP: An implicit generalised interpolation material point method for large deformations, Comput. Struct. 190 (2017) 108–125.
[20] J. Simo, Algorithms for static and dynamic multiplicative plasticity that preserve the classical return mapping schemes of the infinitesimal theory, Comput. Methods Appl. Mech. Engrg. 99 (1992) 61–112.
[21] D.-N. Kim, F. Montáns, K. Bathe, Insight into a model for large strain anisotropic elasto-plasticity, Comput. Mech. 44 (5) (2009) 651–668.
[22] W.M. Coombs, R.S. Crouch, C.E. Augarde, 70-line 3D finite deformation elastoplastic finite-element code, in: T. Benz, S. Nordalm (Eds.), 7th European Conference on Numerical Methods in Geotechnical Engineering, NUMGE, Trondheim, Norway, 2010, pp. 151–156.
[23] W.M. Coombs, Finite Deformation of Particulate Geomaterials: Frictional and Anisotropic Critical State Elasto-Plasticity (Ph.D. thesis), Durham University, 2011.
[24] M. Caminero, F. Montáns, K.-J. Bathe, Modeling large strain anisotropic elasto-plasticity with logarithmic strain and stress measures, Comput. Struct. 89 (2011) 826–843.
[25] E. Lee, D. Lu, Finite-strain elastic-plastic theory with application to plane-wave analysis, J. Appl. Phys. 38 (1967) 19–27.
[26] E. Lee, Elastic-plastic deformation at finite strains, J. Appl. Mech. 36 (1969) 1–6.
[27] J. Simo, R. Taylor, Consistent tangent operators for rate-independent elastoplasticity, Comput. Methods Appl. Mech. Engrg. 48 (1985) 101–118.
[28] C. Miehe, Comparison of two algorithms for the computation of fourth-order isotropic tensor functions, Comput. Struct. 66 (1998) 37–43.
[29] M. Cortis, W.M. Coombs, C.E. Augarde, M.J. Brown, A. Brennan, S. Robinson, Imposition of essential boundary conditions in the material point method, Internat. J. Numer. Methods Engrg. 113 (1) (2018) 130–152.
[30] Z. Wei, D. Perić, D.R.J. Owen, Consistent linearization for the exact stress update of Prandtl-Reuss non-hardening elastoplastic models, Internat. J. Numer. Methods Engrg. 39 (1996) 1219–1235.

[31] R. Krieg, D. Krieg, Accuracies of numerical solution methods for the elastic-perfectly plastic model, J. Pressure Vessel Technol. 99 (1977) 510–515.

[32] B. Loret, J. Prévost, Accurate numerical solutions for Drucker-Prager elastic plastic models, Comput. Methods Appl. Mech. Engrg. 54 (1986) 259–277.

[33] J. Nagtegaal, D. Parks, J. Rice, On numerically accurate finite element solutions in the fully plastic range, Comput. Methods Appl. Mech. Engrg. 4 (1974) 153–177.

[34] J. Simo, M. Rifai, A class of mixed assumed strain methods and the method of incompatible modes, Internat. J. Numer. Methods Engrg. 29 (1990) 1595–1638.

[35] A. Sadeghirad, R.M. Brannon, J. Burghardt, A convected particle domain interpolation technique to extend applicability of the material point method for problems involving massive deformations, Internat. J. Numer. Methods Engrg. 86 (12) (2011) 1435–1456.

[36] A. Sadeghirad, R. Brannon, J. Guilkey, Second-order convected particle domain interpolation (CPDI2) with enrichment for weak discontinuities at material interfaces, Internat. J. Numer. Methods Engrg. 95 (11) (2013) 928–952.

[37] Y. Lian, P. Yang, X. Zhang, F. Zhang, Y. Liu, P. Huang, A mesh-grading material point method and its parallelization for problems with localized extreme deformation, Comput. Methods Appl. Mech. Engrg. 289 (Suppl. C) (2015) 291–315.